Monthly Notices
of the
ROYAL ASTRONOMICAL SOCIETY

MNRAS **506,** 759–774 (2021)
Advance Access publication 2021 June 22

https://doi.org/10.1093/mnras/stab1766

An observational testbed for cosmological zoom-in simulations: constraining stellar migration in the solar cylinder using asteroseismology

Kuldeep Verma [1]★ Robert J. J. Grand [2]★ Víctor Silva Aguirre [1]★ and Amalie Stokholm [1]

[1] *Stellar Astrophysics Centre, Department of Physics and Astronomy, Aarhus University, Ny Munkegade 120, DK-8000 Aarhus C, Denmark*
[2] *Max-Planck-Institut für Astrophysik, Karl-Schwarzschild-Str 1, D-85748 Garching, Germany*

Accepted 2021 June 16. Received 2021 June 10; in original form 2021 February 26

ABSTRACT

Large-scale stellar surveys coupled with recent developments in magneto-hydrodynamical simulations of the formation of Milky Way-mass galaxies provide an unparalleled opportunity to unveil the physical processes driving the evolution of the Galaxy. We developed a framework to compare a variety of parameters with their corresponding predictions from simulations in an unbiased manner, taking into account the selection function of a stellar survey. We applied this framework to a sample of over 7000 stars with asteroseismic, spectroscopic, and astrometric data available, together with six simulations from the Auriga project. We found that some simulations are able to produce abundance dichotomies in the [Fe/H]−[α/Fe] plane which look qualitatively similar to observations. The peak of their velocity distributions match the observed data reasonably well; however, they predict hotter kinematics in terms of the tails of the distributions and the vertical velocity dispersion. Assuming our simulation sample is representative of Milky Way-like galaxies, we put upper limits of 2.21 and 3.70 kpc on radial migration for young ($<$4 Gyr) and old ($\in$[4, 8] Gyr) stellar populations in the solar cylinder. Comparison between the observed and simulated metallicity dispersion as a function of age further constrains migration to about 1.97 and 2.91 kpc for the young and old populations. These results demonstrate the power of our technique to compare numerical simulations with high-dimensional data sets, and paves the way for using the wider field TESS asteroseismic data together with the future generations of simulations to constrain the sub-grid models for turbulence, star formation, and feedback processes.

Key words: asteroseismology – stars: fundamental parameters – stars: kinematics and dynamics – Galaxy: disc – Galaxy: evolution – Galaxy: structure.

1 INTRODUCTION

We are currently in an unprecedented position to understand one of the most important problems of modern astrophysics, viz. the formation and evolution of our host Galaxy, the Milky Way. On the one hand, we have rich observational stellar data for a significant fraction of the whole sky from various ground- and space-based instruments; for instance spectroscopic data from the RAVE, LAMOST, *Gaia*-ESO, GALAH, and APOGEE surveys (see e.g. Steinmetz et al. 2006; Gilmore et al. 2012; Zhao et al. 2012; De Silva et al. 2015; Majewski et al. 2017), astrometric data from the *Gaia* mission (see e.g. Gaia Collaboration 2016, 2018), and asteroseismic data from the *Kepler*/K2 and TESS satellites (see e.g. Gilliland et al. 2010; Howell et al. 2014; Ricker et al. 2014). Specifically, asteroseismology enables us to measure stellar ages to precision better than 20 per cent (see e.g. Silva Aguirre et al. 2020). These data contain complex signatures of the key events taking place in the assembly history of the Galaxy. On the other hand, we now have cosmological magneto-hydrodynamical zoom-in simulations of the formation of Milky Way-mass galaxies (see e.g. Grand et al. 2017), which help us in accurately interpreting the observations and provide important insights into the physical processes which played critical role in the evolutionary history of the Milky Way.

The early stellar counts in the solar-neighbourhood indicated the presence of two distinct groups of stars: (1) the thin disc stars that were distributed in the Galactic plane with a vertical scale height of about 300 pc, and (2) the thick disc stars that were distributed with a scale height of approximately 900 pc (Gilmore & Reid 1983; Jurić et al. 2008). Typically, the structural thin and thick disc stars have different characteristics in terms of chemistry and kinematics (see e.g. Fuhrmann 1998; Bensby, Feltzing & Lundström 2003; Feltzing, Bensby & Lundström 2003; Soubiran, Bienaymé & Siebert 2003; Holmberg, Nordström & Andersen 2009; Lee et al. 2011; Adibekyan et al. 2013; Bensby, Feltzing & Oey 2014). Stars also appear in two distinct sequences in the [Fe/H]−[α/Fe] plane: the high-α sequence is traditionally called chemical thick disc while the low-α sequence is dubbed chemical thin disc (see e.g. Recio-Blanco et al. 2014; Nidever et al. 2014; Hayden et al. 2015; Mikolaitis et al. 2017). There is a clear age difference between the high- and low-α sequence stars, the former being older than the later, as demonstrated by e.g. Silva Aguirre et al. (2018) using the *Kepler* asteroseismic data. It should be noted that the structural, chemical, and kinematic separations of the thin and thick discs are not the same thing (see e.g. Hayden et al. 2017). In fact, Hayden et al. (2015) showed that stars belonging to the low-α sequence lie high above the disc mid-plane outside the solar radius, which was later explained

★ E-mail: kuldeepv89@gmail.com (KV); grand@mpa-garching.mpg.de (RJJG); victor@phys.au.dk (VSA)

as the flaring of mono-age populations by Minchev et al. (2015). The latter work explained a number of seemingly contradictory observations regarding thick disc formation by introducing nested flares of mono-age stellar populations. Furthermore, it predicted a strong age gradient in the structural thick disc, which was verified using APOGEE data by Martig et al. (2016). Such complex signatures in the spectroscopic, kinematic, and asteroseismic data can be used to unravel the formation and evolution history of the Milky Way discs through Galactic archaeology (see Freeman & Bland-Hawthorn 2002; Rix & Bovy 2013; Bland-Hawthorn & Gerhard 2016).

Over the past couple of decades, the computational advancement in terms of resources and numerical methods have led to the development of realistic hydrodynamical simulations of the formation of disc galaxies in the full cosmological context (see e.g. Okamoto et al. 2005; Brooks et al. 2011; Guedes et al. 2011; Aumer et al. 2013; Stinson et al. 2013a; Marinacci, Pakmor & Springel 2014; Wang et al. 2015; Grand et al. 2017; Naab & Ostriker 2017). These Milky Way-mass simulations can qualitatively reproduce a number of observables for the Milky Way, such as flat rotation curve, disc scalelength, star formation rates (both the histories and present-day values), structural thin and thick disc components' scale heights, as well as resolving morphological features like spiral arms and bars. The high- and low-α disc dichotomy has also been observed in cosmological simulations, and various possible formation scenarios have been discussed (see e.g. Brook et al. 2012; Grand et al. 2018a; Agertz et al. 2020; Buck 2020).

Although there have been qualitative comparisons between a few selected observables of the Milky Way with corresponding predictions of cosmological simulations (see e.g. House et al. 2011; Stinson et al. 2013b; Gómez et al. 2016; Minchev et al. 2017; Fattahi et al. 2019; Fragkoudi et al. 2020; Grand et al. 2020), a systematic study involving observations from a large stellar survey is challenging primarily because of the involved selection functions associated with the observing instruments. A notable work in this direction was carried out by Anders et al. (2017) using the CoRoT (Baglin et al. 2006; Michel et al. 2008) and APOGEE data and chemodynamical model (Minchev, Chiappini & Martig 2013, 2014; Anders et al. 2016). They made an attempt to take into account the selection function by simply selecting stars randomly from small boxes in the colour–magnitude diagram. In this work, we go beyond the study by Anders et al. (2017) by including distances along with colour and magnitude in our selection function. Moreover, we demonstrate how closely we reproduce the observed selection function. In other words, we develop a framework – taking into account proper selection function – in which we can systematically compare any observed/inferred set of stellar properties coming from e.g. spectroscopic, photometric, asteroseismic, and astrometric surveys with the predictions of the Auriga suite of cosmological simulations by Grand et al. (2017). This enables us to identify the parameter-specific discrepancies between the observation and simulations, and hence systematically point out the model aspects that need amendments.

Stars are known to move radially in and out in the Galactic disc due to angular momentum transfer and scatterings. Frankel et al. (2018, 2020) used parametrized models together with APOGEE data to estimate radial stellar migration. Minchev et al. (2018) used age and metallicity from HARPS data to find the birth places of stars. Thanks to the added dimension of precise asteroseismic ages, we demonstrate how we can use the observations in this framework to constrain the extent of radial migration of stars in the solar cylinder.

Since cosmological simulations are computationally expensive, we produce a lower resolution model variation for one of the halo in the Auriga sample to illustrate how this study can be extended in the future to help constrain and improve galaxy formation models. This whole framework can be used in the future as a testbed for any larger suite of cosmological simulations with different sub-grid galaxy formation models for turbulence, star formation, and feedback processes to unravel the formation history of the Milky Way.

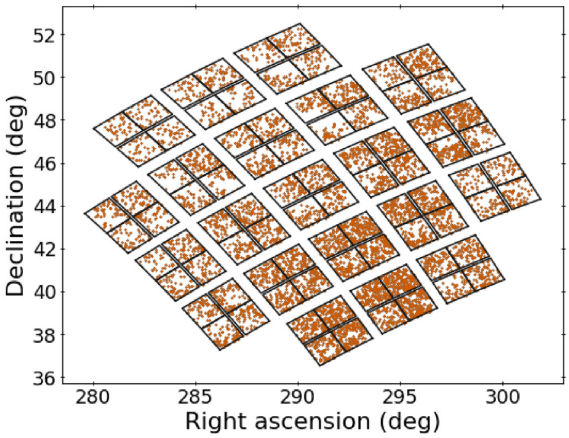

Figure 1. Spatial distributions of stars in the *Kepler* field.

2 THE OBSERVED SAMPLE

We have a total of 7186 targets in the observed sample used in this study. These stars were all observed by the *Kepler* spacecraft during its nominal mission (Gilliland et al. 2010; Koch et al. 2010). In Fig. 1, the targets are shown in the fixed *Kepler* field of view. We retrieved the global asteroseismic quantities, namely the frequency of maximum power, $\nu_{\rm max}$, and the large frequency separation, $\Delta\nu$, from Yu et al. (2018). We used the solutions found by the SYD pipeline (Huber et al. 2009) to be consistent with the solar values of $\nu_{\rm max}$ and $\Delta\nu$ used in the stellar properties determination (see further details below).

All stars have chemical abundances available from the 16th data release of the Apache Point Observatory Galactic Evolution Experiment (APOGEE DR16; Majewski et al. 2017; Ahumada et al. 2020), along with measured JHK_s-band photometric magnitudes from the Two Micron All-Sky Survey (2MASS; Skrutskie et al. 2006). We also have six-dimensional astrometric measurements (celestial positions, proper motions, parallax and line-of-sight velocity) for all stars in our sample from the second data release of *Gaia* (*Gaia* DR2; Gaia Collaboration 2018). The systematic zero-point offset for the *Gaia* DR2 parallaxes (Lindegren et al. 2018) was corrected following Zinn et al. (2019) as their correction was computed based on similar stars within the *Kepler* field of view.

Besides requiring the availability of the above information for all stars, we also had the following quality criteria applied in this work:

(i) The 2MASS quality flag `Qflg` $=A$ for all bands.
(ii) No `TEFF_BAD` or `VMICRO_BAD` ASPCAP flag set in APOGEE.
(iii) No `LOW_SNR`, `PERSIST_JUMP_POS`, `PERSIST_JUMP_NEG`, `SUSPECT_RV_COMBINATION`, `VERY_BRIGHT_NEIGHBOR` or `PERSIST_HIGH` star flag set in APOGEE.
(iv) $\varpi > 0$ and $\varpi/\sigma_{\varpi} > 5$, where ϖ and σ_{ϖ} denote the parallax and its uncertainty, respectively.

We note that removing the positive parallaxes with inverse fractional uncertainties above a threshold as well as negative parallaxes can bias the sample (Luri et al. 2018). However, since we compare it with simulation samples cut in the same way, this bias is not an issue in this study.

The stellar properties, including ages for the sample were determined using the BAyesian STellar Algorithm (BASTA; Silva Aguirre et al. 2015, 2017). Briefly, BASTA uses a Bayesian approach and computes the probability density functions for stellar properties by combining a set of stellar models with the observational constraints and prior information. In this study, we used the BaSTI (a Bag of Stellar Tracks and Isochrones) stellar models and isochrones library (Hidalgo et al. 2018) with overshooting and no mass-loss. For the reference solar values, we adopted $\nu_{\max,\odot} = 3090\,\mu$Hz, $\Delta\nu_\odot = 135.1$ μHz (Huber et al. 2011), and effective temperature $T_{\rm eff,\odot} = 5777$ K. We used the Salpeter initial mass function (Salpeter 1955) as a prior to quantify our expectation of mostly low-mass stars. Furthermore, we constrained the ages of our stars to be within the age of the Universe (13.6 Gyr; to be consistent with the simulations). For all stars in our sample, we fitted the effective temperature $T_{\rm eff}$, metallicity [Fe/H], large frequency separation $\Delta\nu$ (corrected following the prescription of Serenelli et al. 2017), frequency of maximum power $\nu_{\max}$, the corrected parallax ϖ along with apparent magnitudes in the 2MASS JHK_s photometric bands using the Green et al. (2019) dust map to account for extinction. In addition, asteroseismology can inform us whether a red giant star is burning hydrogen in the shell or helium in the core (see e.g. Bedding et al. 2011). We used the evolutionary phase information available from asteroseismology as a Bayesian prior in determining the stellar properties. The resulting stellar ages have a median uncertainty of about 16 per cent (which is a conservative estimate because we symmetrized the errorbar by using the maximum of the negative and positive uncertainties).

3 THE AURIGA SIMULATIONS AND MOCK CATALOGUES

The Auriga project[1] includes a suite of 30 high-resolution cosmological magneto-hydrodynamical zoom-in simulations of the formation of Milky Way-mass galaxies (see Grand et al. 2017). Following the naming convention used in the original paper, we shall refer the simulations as Au01, Au02, ..., Au30 in this study. The simulations were performed using a moving-mesh, *N*-body, magneto-hydrodynamics code (AREPO; Springel 2010). We refer the reader to the paper by Grand et al. (2017) for further details on the model physics considered as well as on the physical properties of all the 30 simulated galaxies. Briefly, the computation of an Auriga zoom simulation involves the following steps.

(i) Identify an isolated host dark matter halo of virial mass lying within the range $[1 \times 10^{12}, 2 \times 10^{12}]$ $M_\odot$ at the redshift $z = 0$ from the Eagle dark matter only simulation by Schaye et al. (2015).

(ii) Trace the halo back in time at $z = 127$. Subsequently, split the dark matter into the dark and baryonic components according to the measured parameters of the standard Lambda cold dark matter model of big bang cosmology (Planck Collaboration XVI 2014).

(iii) Increase the resolution of the Lagrangian region around the halo, and degrade the resolution of distant particles.

(iv) Evolve it back to $z = 0$ using the AREPO code with a comprehensive galaxy formation model.

Despite a significant advancement in computational resources during the past a couple of decades, current hydrodynamical simulations of galaxy formation cannot resolve individual stars. The mass resolutions of the dark and baryonic matter particles in the Auriga simulations are about 4×10^4 and 5×10^3 $M_\odot$, respectively. A star particle in the simulation represents a single stellar population of a given age and metallicity. Following two different approaches (as described below), Grand et al. (2018b) presented mock *Gaia* DR2 stellar catalogues for six simulations (Au06, Au16, Au21, Au23, Au24, and Au27) that had distinct properties. Specifically, they selected Au16 and Au24 for their large discs; Au06 for being a close Milky Way analogue in terms of stellar mass, star formation rate, thin and thick discs' scale heights, and morphology; and Au21, Au23, and Au27 for their interesting satellite interactions.

The process of generating mock catalogues requires specification of the solar position and velocity. Grand et al. (2018b) presented four mock catalogues for each of the above six simulations with four different solar positions spread at equidistant azimuthal angles. They chose their reference solar azimuth at 30 deg behind the major axis of the bar (the corresponding catalogue is referred to as the reference catalogue), while other three positions were assumed at 120, 210, and 300 deg behind the bar. The distance between the Sun and Galactic centre was assumed to be 8 kpc (Reid 1993), and the Sun's height above the Galactic plane, 20 pc (Humphreys & Larsen 1995). They assumed the solar velocity with respect to the local standard of rest to be [11.1, 12.24, 7.25] km s^{-1} (Schönrich, Binney & Dehnen 2010). Grand et al. (2018b) created mock catalogues following two different approaches: (1) using the parallelized version of SNAPDRAGONS code (HITS-MOCKS; Hunt et al. 2015), and (2) using the method described in Lowing et al. (ICC-MOCKS; 2015). This means that we have a total of eight catalogues for each simulation. In this study, we shall use the ICC-MOCKS as reference, whereas the HITS-MOCKS for Au06 will be used to assess the robustness of our conclusions against the uncertainties associated with methods used to generate mock catalogues. We refer the reader to Grand et al. (2018b) for a detailed discussion on the limitations of the two mocks as well as advantages of one over the other.

The different mock catalogues for all the six simulations are publicly available.[2] The catalogues provide several quantities including astrometric and photometric parameters, radial velocity, stellar properties, and their uncertainties. A complete list of parameters contained in the catalogues can be found in table A1 of Grand et al. (2018b). The mock catalogues also contain unique ID of the parent simulation particle, which can be used to extract more information about star particles – such as elemental abundances, birth position, and birth velocity – from the snapshots.

We analyse also a model variation for Au06 that includes: (i) a softer equation of state (EOS) for the sub-grid interstellar medium (ISM) model (Vogelsberger et al. 2013); (ii) a metallicity-dependent wind velocity prescription (see e.g. equation 3 of Pillepich et al. 2018); and (iii) a thermal and kinetic active galactic nucleus jet feedback model (Weinberger et al. 2017). The soft EOS interpolates between an isothermal equation of state and the full (Springel & Hernquist 2003) effective equation of state, with an interpolation parameter $q = 0.3$. This describes a case in which a fraction of the stellar feedback energy is retained by the ISM, resulting in a less pressurised ISM relative to the fiducial case. The metal-dependent wind scheme adopts a scaling that relates the velocity of galactic winds with gas metallicity, motivated by additional radiative losses

[1] https://wwwmpa.mpa-garching.mpg.de/auriga/

[2] http://dataweb.cosma.dur.ac.uk:8080/gaia-mocks/

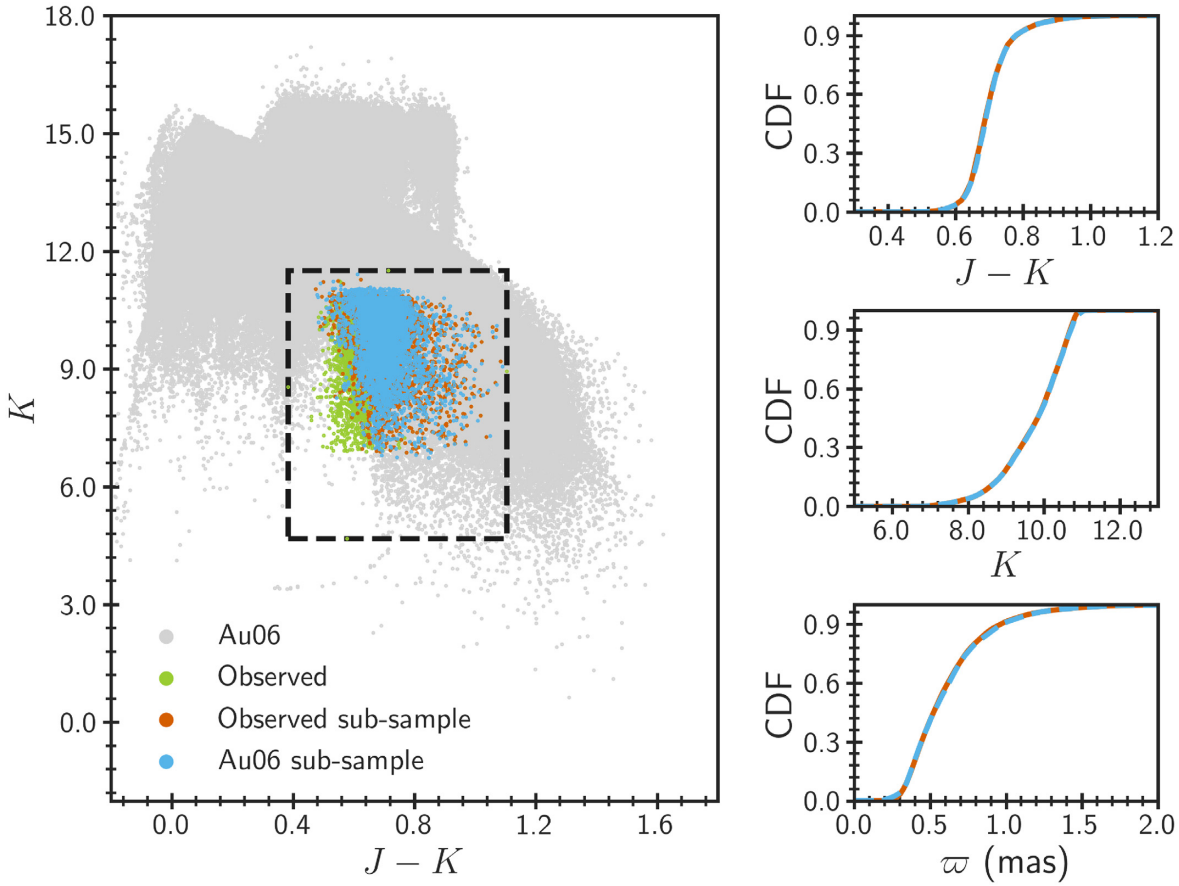

Figure 2. Illustration of the selection function using the Au06 ICC catalogue generated assuming the standard solar azimuth. The left-hand panel shows the colour–magnitude diagram for Au06 stars in the *Kepler* field of view (grey dots), observed stars (green dots), sub-sampled observed stars (orange dots), and sub-sampled Au06 stars (blue dots). The rectangular box encloses all the observed stars. The right-hand panels demonstrate the cumulative distribution functions of the sub-sampled observed (orange solid curve) and sub-sampled Au06 stars (blue dashed curve) for the colour (top panel), magnitude (middle panel), and the parallax (bottom panel). See the corresponding text for details.

implied by higher metallicity galaxies (e.g. Schaye et al. 2015). This simulation is lower in resolution by a factor of about 8 in mass, and the corresponding HITS mock catalogue was generated using the SNAPDRAGONS code (Hunt et al. 2015). Hereafter, we refer to this simulation as soft EOS to distinguish it from the fiducial Auriga model simulations.

4 THE SELECTION FUNCTION

In this study, we aim to perform direct comparisons between observations and simulations. However, before we can do such comparisons sensibly we need to carefully account for the biases in the observations. The observed sample used in the current study is biased mainly for three reasons. First, unlike simulations the data set is spatially limited to the *Kepler* field of view (see Fig. 1). This is straightforward to deal with because we can easily extract the stars from simulations that are in the *Kepler* field of view and perform the comparisons. Secondly, the sample is limited due to the Malmquist bias (or selection bias), i.e. only intrinsically brighter stars can be observed at larger distances. Finally, the observed sample is biased because the *Kepler* stars were selected based on a number of heterogeneous criteria (Huber et al. 2010; Pinsonneault et al. 2014). The combined effect of the last two is substantially more complicated.

A careful account of such biases is also necessary when studying the structural properties of the Milky Way using observed stellar populations. For example, Casagrande et al. (2016) used photometry to derive the colour and magnitude limits within which their asteroseismic sample was representative of an underlying unbiased photometric sample. Moreover, they used several different approaches, including population synthesis and Galaxy modelling, to account for the *Kepler* target selection. We note that the inferences of physical properties of the Milky Way, as done in the above studies, ideally require observation of the true underlying stellar populations. However, this is not the case for our specific problem at hand: we can make meaningful comparisons between the observation and simulations and draw conclusions even if they are biased (as long as both are biased in the same way).

In this study, we take a slightly different approach, in which we sub-sample simulation stars based on the observation, ensuring similar biases in both. This is done by first extracting all the simulation stars from the *Kepler* field of view. Similar to the observation, we consider only those simulation stars that have reliable parallaxes, i.e. the stars with positive parallaxes and with their inverse fractional uncertainties greater than 5. In the colour–magnitude diagram shown in the left-hand panel of Fig. 2, these stars are shown in grey for the reference ICC catalogue for Au06. To ensure similar biases, we sub-sample stars from both the observation and simulation in such a

way that their distributions of $J-K$ colour, K magnitude, and ϖ are similar. This process is explained below in more detail using example of the reference ICC catalogue for Au06.

To improve the computational efficiency, we first discard all the Au06 stars outside the observed ranges in $J-K$ colour, K magnitude, and parallax. For simplicity, this is illustrated in the projected 2D space in the left-hand panel of Fig. 2. We get rid of the Au06 stars outside the rectangular box, which encloses all the observed stars as shown with the green dots. Subsequently, we discretize the resulting datacube with $n_{J-K}+1$, n_K+1, and $n_\varpi+1$ uniformly spaced points along the $J-K$, K, and ϖ dimensions, respectively. This divides the full observed space into $n_{J-K}\times n_K\times n_\varpi$ small sub-spaces (or cells). For each cell, we randomly choose as many Au06 stars as there are observed in that cell. Note that a simulation of the Milky Way should ideally produce a number of stars in each cell which is greater than or equal to the number of observed stars in that cell. In reality however, the models of galaxy formation are uncertain, resulting in fewer simulation stars in some cells compared to the observation. For such cells, we randomly choose as many observed stars as there are Au06 stars in that cell, i.e. disregard some of the observed stars as well.

By construction, the above process results in two sub-samples – one of the observed sample and the other of Au06 mock catalogue – of same size. Clearly, the sub-samples also have similar distributions in $J-K$ colour, K magnitude, and parallax. The similarities of the distributions depend on the choice of the number of points along each dimension: the larger the number of points, the more similar the distributions. Since the choice of arbitrarily large numbers for n_{J-K}, n_K, and n_ϖ reduces sub-samples' size significantly, we find their optimal values through an iterative process, which involves the following steps.

(i) Initialize $n_{J-K}=5$, $n_K=5$, and $n_\varpi=5$.
(ii) Find the sub-samples of the observed sample and Au06 mock catalogue following the procedure described above.
(iii) Assess similarities of the distributions of $J-K$ colour, K magnitude, and ϖ from the two sub-samples using K-sample Anderson–Darling test.
(iv) Increase the number of points along the dimensions by 5 if the corresponding null hypotheses – that the two sub-samples are drawn from the same distribution – are rejected at the 5 per cent level, and repeat from step (ii).

Following the above process, we found that the null hypotheses could not be rejected for $n_{J-K}=30$, $n_K=25$, and $n_\varpi=40$. The corresponding observed and Au06 sub-samples are shown in orange and blue dots in the left-hand panel of Fig. 2, and the cumulative distribution functions (CDFs) for the colour, magnitude, and parallax are compared in the right-hand panels.

In Fig. 3, we show the spatial distributions of stars in the observed and Au06 sub-samples. As expected, both the observed and simulation stars are from the same region in the Milky Way. Moreover, there is a reasonable agreement between the distributions of the observed and simulation stars in the $R-z$ plane. Fig. 4 compares the two sub-samples in the Kiel diagram. Clearly, the stars in the two sub-samples have similar spectral type. The above ensures that we can now use the two sub-samples, and make meaningful comparisons. It should be noted that we go through the above process before comparing any of the simulation mock catalogues with the observation, which means we shall implicitly work with sub-samples in the subsequent sections (unless stated explicitly otherwise). On average, our resulting sub-samples contain about 5200 stars compared to the original 7186 observed targets.

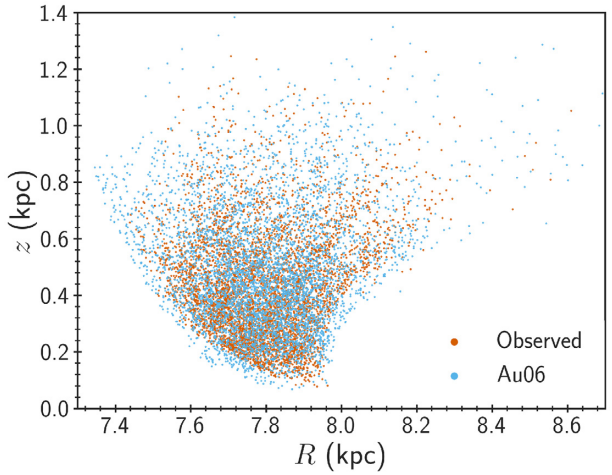

Figure 3. Spatial distributions of the observed (orange) and Au06 (blue) stars after the selection function.

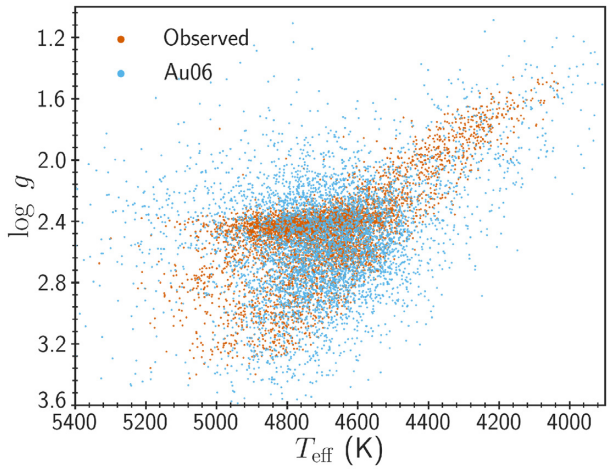

Figure 4. Kiel diagrams for the observed (orange) and Au06 (blue) stars after the selection function.

5 RESULTS

We applied the selection function described in Section 4 to all four ICC catalogues generated assuming solar azimuths at 30, 120, 210, and 300 deg behind the major axis of the bar for each of the six simulations (Au06, Au16, Au21, Au23, Au24, and Au27), as well as to the all four HITS catalogues generated for the Au06 simulation. This results in a total of 28 pairs of samples (one pair corresponding to each mock catalogue). The final sample size after the selection function for all pairs is listed in Table 1, which varies from 4262 to 6165 depending on the simulation and mock catalogue. In the next few sub-sections, we shall compare the predictions of simulations with the observation.

5.1 Comparison of the abundance distributions in [Fe/H]−[α/Fe] plane

The α-elements primarily form from core collapse supernovae on Myr time-scales while iron forms mainly from Type Ia supernovae on Gyr time-scales (see e.g. Matteucci & Greggio 1986). This makes the abundance plane [Fe/H]−[α/Fe] particularly interesting: it is now well known that this plane contains key information about the

Table 1. The final sample size after selection function and the estimated radial stellar migration. The columns are divided into four groups based on the solar azimuths assumed in generating mock catalogues. The size is the number of stars in the sample. The $\Delta R_{<4}$ and $\Delta R_{\in[4,8]}$ denote radial migrations for young (<4 Gyr) and old ($\in$[4, 8] Gyr) stellar populations, respectively.

Simulation	The Sun at 30 deg			The Sun at 120 deg			The Sun at 210 deg			The Sun at 300 deg		
	Size	$\Delta R_{<4}$ (kpc)	$\Delta R_{\in[4,8]}$ (kpc)	Size	$\Delta R_{<4}$ (kpc)	$\Delta R_{\in[4,8]}$ (kpc)	Size	$\Delta R_{<4}$ (kpc)	$\Delta R_{\in[4,8]}$ (kpc)	Size	$\Delta R_{<4}$ (kpc)	$\Delta R_{\in[4,8]}$ (kpc)
Au06(ICC)	5216	1.99	2.03	4782	1.42	2.09	5143	1.94	2.06	5453	1.17	1.91
Au16(ICC)	4299	1.05	3.09	4478	1.32	3.11	4262	1.11	3.35	4270	0.86	3.13
Au21(ICC)	5510	1.82	2.92	5456	1.90	3.04	5396	1.95	2.81	5679	2.21	2.87
Au23(ICC)	5246	1.69	2.74	5868	1.78	2.45	5334	2.12	2.32	5313	1.68	2.57
Au24(ICC)	4455	2.08	3.52	4675	1.38	3.32	4663	1.13	3.70	4354	1.54	3.53
Au27(ICC)	6008	1.66	2.43	5769	1.31	2.36	5524	1.24	2.25	5636	1.08	2.24
Au06(HITS)	5805	1.99	2.03	4995	1.23	2.17	5777	1.75	2.13	6165	1.22	1.99

formation and evolution of the Galactic discs (see e.g. Matteucci 2012; Andrews et al. 2017). For instance, the observed high- and low-α sequences in this plane can be explained by the so-called two-infall chemical evolution models (see e.g. Spitoni et al. 2019, 2020, 2021), which hypothesized that there were two episodes of gas accretion at two different epochs (well separated in time) in the formation history of the Milky Way. On the other hand, a similar distribution in the abundance plane can be produced with analytical chemodynamical models including effects of radial migration and kinematic heating, as recently shown by e.g. Sharma, Hayden & Bland-Hawthorn (2020).

In Fig. 5, we compare the abundance predictions from the Auriga simulations with the observation in [Fe/H]−[Mg/Fe] plane. We assume the [Mg/Fe] abundance ratio to be the tracer of α-element abundances. It is well known that simulations using yields from Portinari, Chiosi & Bressan (1998), as is the case for the Auriga simulations, underproduce magnesium by a factor of about 2.5 (see e.g. van de Voort et al. 2020). Therefore, we corrected the magnesium abundance by this factor. We wish to point out that, since magnesium is not a strong coolant, its underproduction is not expected to affect the dynamics of simulations. We note that distributions of the observed stars differ slightly from one panel to another because of the selection function (see Section 4). A dichotomy can easily be seen in the observed abundances. We can see a variety of predicted distributions in different panels, some of which also show a dichotomy with different morphology. The predicted dichotomy for Au27 is particularly similar to the observed one. Qualitatively, the results are similar for the HITS catalogues (see Fig. A1) and for the catalogues generated assuming different solar azimuths (see Figs A2–A4), although some differences may also be noticed.

Although some simulations do produce abundance dichotomy, there are several differences between the distributions of the observed and simulated abundances. For instance, all simulations seem to predict systematically larger [Fe/H] compared to the observation. Moreover, there are clear morphological differences between the observed dichotomy and the closest matching dichotomy for Au27. These differences are likely related to the used input physics in the Auriga simulations, in particular they are expected to depend on the assumed yields and feedback processes. The suite of Auriga simulations used yields from Karakas (2010) for asymptotic giant branch stars and from Portinari et al. (1998) for core collapse supernovae. Certain features of the abundance distribution predicted by the recent VINTERGATAN simulation, which uses the yields from Woosley & Heger (2007), appear to agree slightly better with the observations. For instance, their predicted [Fe/H] is less than 0.6 (see fig. 15 of Agertz et al. 2020). However, they have similar issue with the oxygen abundance, which is overproduced in the simulation.

To test if we can improve our simulations, we produced a model variation for Au06 as discussed in Section 3. As shown in the top left panel of Fig. 5, this model avoids the issue of large metallicity predicted by the fiducial Auriga simulations. We can use our framework in the future for new simulations with yields from different sources and with various sub-grid models for feedback processes (e.g. Agertz et al. 2020; Buck 2020; Buck et al. 2021) to better understand the chemical evolution of the Milky Way in full cosmological context.

5.2 Comparison of the velocity distributions

We used the 6D phase-space information of the observed sample and simulation mock catalogues to compute their Galactocentric velocity in cylindrical coordinates using ASTROPY[3] (Astropy Collaboration 2013, 2018). To be consistent, we used the same solar position and velocity in the transformation as used by Grand et al. (2018b) in generating the mock catalogues.

In Fig. 6, we compare velocity distributions predicted by the Auriga simulations with the corresponding distributions of the observed samples. Recall from Section 4 that we get a slightly different observed sample due to the selection function depending on the simulation mock catalogue at hand for comparison. In Fig. 6, the different orange curves (which are very similar and hence overlap substantially) show velocity distributions for observed sub-samples corresponding to the six simulation mock catalogues. As we can see in the figure, for all of the three velocity components, the peaks of the distributions for the observation and simulations agree reasonably well. However, all six simulations predict much longer tails in the velocity distributions compared to the observed sample. This systematic difference is likely due to inaccuracies in the currently used sub-grid models for turbulence, star formation and feedback processes in the Auriga project, which can be tested in the future by comparing simulations generated using revised recipes of these physical processes (as discussed further in this section below) with the observation.

Fig. 7 shows the vertical velocity dispersion as a function of age. We used the so-called biweight mid-variance – a robust statistic as implemented in ASTROPY with standard tuning constant, $c = 9$ – to determine the velocity variance (square root of which gives the velocity dispersion). Again, the orange curves in the figure show the velocity dispersion for all of the six observed sub-samples. As we can see in the figure, all of the six simulations predict substantially 'hotter' kinematics compared to the Milky Way. The above results

[3] https://www.astropy.org

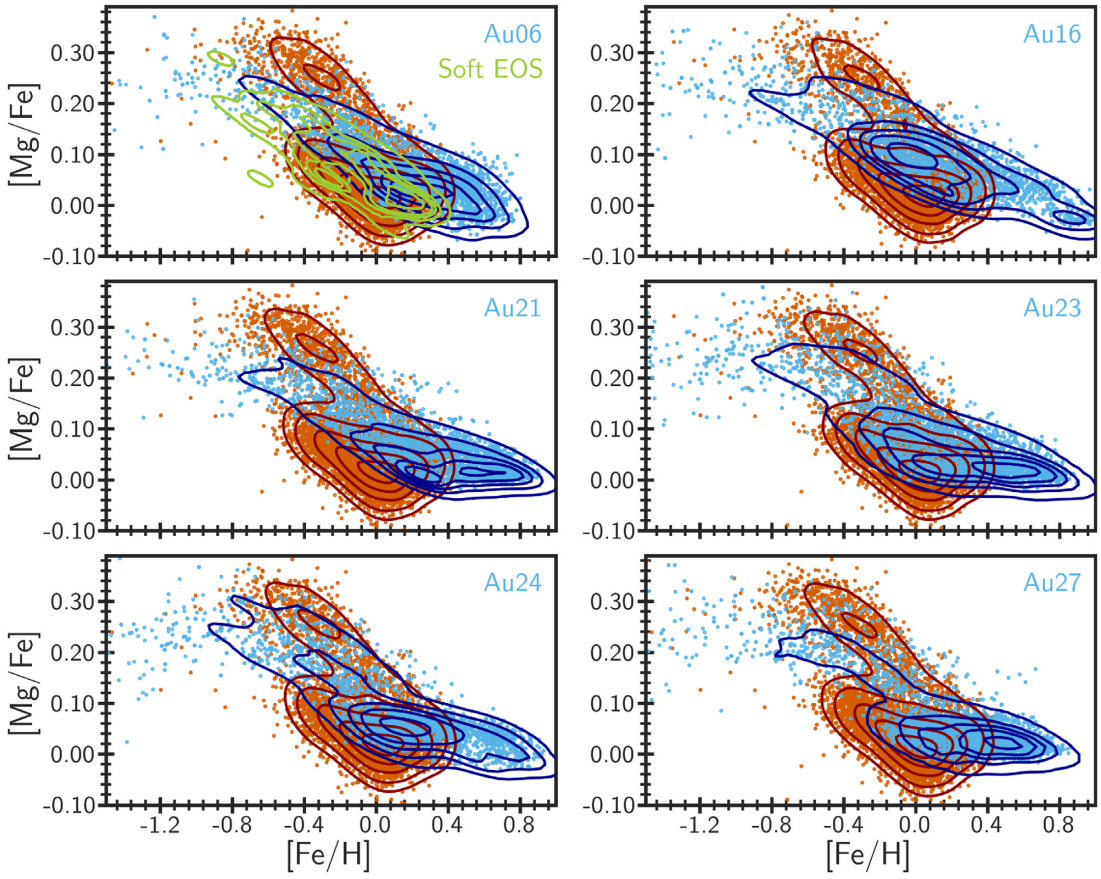

Figure 5. Comparison between the observed and simulation abundance distributions in [Fe/H]−[Mg/Fe] plane. The six different panels correspond to different simulations with the respective ICC catalogue generated assuming the standard solar azimuth. In each panel, the orange and blue dots represent the observed and simulation stars, respectively, while the five dark red (blue) innermost-to-outermost contours enclose approximately 10, 30, 50, 70, and 90 per cent of the observed (simulation) stars. In top left panel, the green contours show the model variation for Au06 as discussed in Section 3. The corresponding dots are not shown for the sake of clarity.

are qualitatively independent of the choice of mock catalogues (see Fig. A5 for results obtained using HITS catalogues) and also the solar azimuths assumed in generating the mock catalogues (see Figs A6–A8 for results obtained assuming solar azimuths 120, 210, and 300 deg, respectively).

This is a well-known issue related to cosmological simulations. House et al. (2011) used seven cosmological simulations run with different *N*-body hydrodynamical galaxy formation codes to study the age–velocity dispersion relation (AVDR) for disc stars. They concluded that all of the analysed simulations predict too large velocity dispersions compared to the Milky Way disc. House et al. (2011) pointed out that the velocity dispersion of a simulation has a lower limit which depends on the treatment of the heating and cooling of the interstellar medium, and on the assumed density threshold for star formation.

Traditionally, cosmological zoom-in simulations used small values of the star formation density threshold compared to the typically observed densities of star-forming regions (density of a giant molecular cloud $\sim$100 cm^{-3}). For example, Governato et al. (2007) and House et al. (2011) used a density threshold of 0.1 cm^{-3}. This was mainly because those simulations could not resolve the observed densities of star-forming regions. The Auriga simulations used a density threshold of 0.13 cm^{-3} (Grand et al. 2017), which was derived from the parameters describing the ISM and the desired star formation time-scale (Springel & Hernquist 2003). Recently, Bird et al. (2020) used the high-resolution cosmological zoom-in simulation `h277` from Christensen et al. (2012) to closely reproduce the measured solar-neighbourhood AVDR of Casagrande et al. (2011). They attributed this success mainly to the simulation's ability to form stars in dense and cold environment ($n > 100$ cm^{-3} and $T < 1000$ K, where n and T are number density and temperature, respectively), similar to those in giant molecular clouds. Although these results are indeed promising, several aspects (and not just the density threshold) of the sub-grid galaxy formation physics affect the resulting velocity dispersion. In fact, simulations have been carried out with a density threshold as large as 1000 cm^{-3} which still result in too hot kinematics (Sanderson et al. 2020).

Our preliminary test with softer equation of state produces velocity distributions and AVDR that are in better agreement with the observations (compare solid green and orange curves in Figs 6 and 7). We can use our framework together with precise asteroseismic ages in the future to distinguish between the various possible physical scenarios relevant in the formation of the Milky Way.

5.3 Constraining radial stellar migration in the solar cylinder

Stars move radially in and out in the Galactic disc due to angular momentum transfer ('churning'), for instance from the bar and spiral arms, as well as due to scattering ('blurring'), for example from giant molecular clouds (see Sellwood & Binney 2002; Roškar et al. 2008;

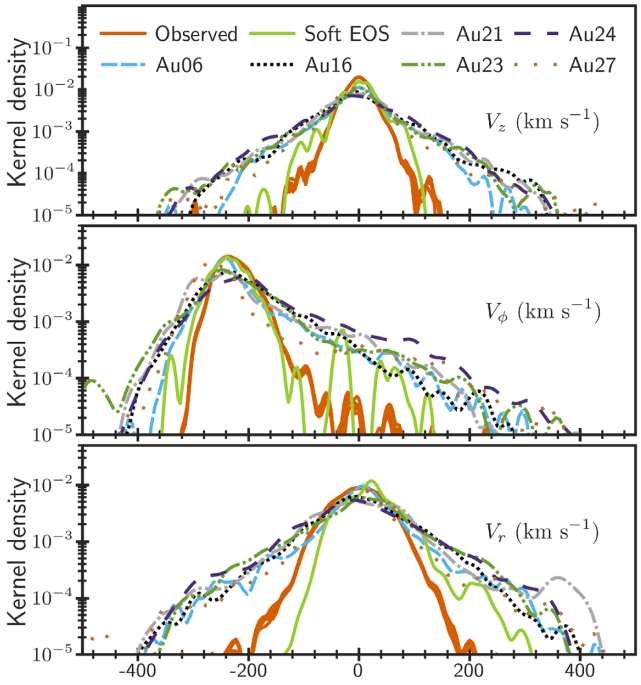

Figure 6. Comparison between the observed and simulation Galactocentric velocity distributions. The top, middle, and bottom panels show the vertical, azimuthal, and the radial components of the velocity distributions in cylindrical coordinate, respectively. In each panel, solid orange curves represent observed samples (see the corresponding text for details), while the other curves correspond to the six simulations (see the legend in the top panel) with the respective ICC catalogue generated assuming the standard solar azimuth. The solid green curves show the model variation for Au06 as discussed in Section 3.

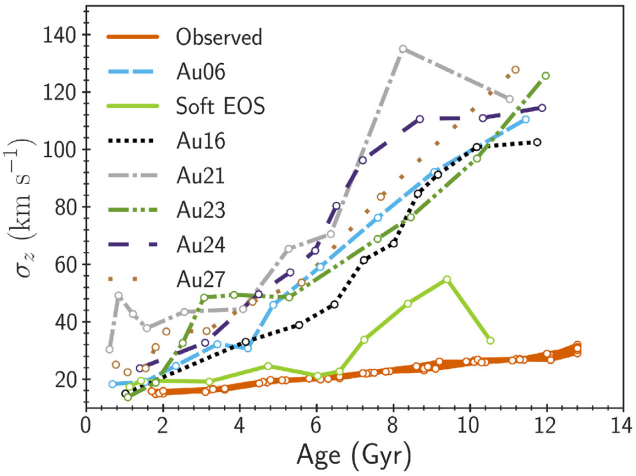

Figure 7. Comparison between the observed and simulation age–velocity dispersion relation. Solid orange curves represent observed samples (see the corresponding text for details), while the other curves correspond to the six simulations (see the legend) with the respective ICC catalogue generated assuming the standard solar azimuth. The solid green curve shows the model variation for Au06 as discussed in Section 3. The uncertainties in the observed data were propagated to the computed velocity dispersion using Monte Carlo simulation (uncertainties lie within the thickness of orange curves). The age bins were chosen in such a way that they contain approximately same numbers of stars.

Schönrich & Binney 2009; Minchev & Famaey 2010; Minchev et al. 2013; Grand, Kawata & Cropper 2015). The radial diffusion of stars caused by churning is known as radial stellar migration, whereas the one caused by blurring is termed kinematic or radial heating.

There have been attempts to measure the strength of radial migration, as well as to quantify its importance in shaping the Galactic disc in comparison to kinematic heating. For instance, Sanders & Binney (2015) used action- and metallicity-based analytic distribution functions with a prescription for radial migration to fit the solar-neighbourhood chemodynamical data (Geneva-Copenhagen Survey; Nordström et al. 2004) and the stellar density data (Gilmore & Reid 1983). They found the dispersion of angular momentum, σ_L, for 12 Gyr old stellar populations to be 1150 kpc km s^{-1} (which can be translated to 939 kpc km s^{-1} for 8 Gyr old populations using the relation $\sigma_L = 1150\sqrt{\tau/12}$, where τ is the age of the population). Assuming a solar circular velocity of 235 km s^{-1}, this gives a radial migration of about 4.0 kpc for 8 Gyr old populations. Using the basic ideas from Sanders & Binney (2015) and Frankel et al. (2018) developed a simple model by parametrizing the relevant physical processes including radial migration, and fitted it to the APOGEE DR12 (Alam et al. 2015) low-α red clump stars. They found global radial migration of 3.6 $\pm$ 0.1 kpc for 8 Gyr old populations. By generalizing the model of Frankel et al. (2018) in the direction of Sanders & Binney (2015) and using the data from APOGEE DR14, Frankel et al. (2020) investigated the relative contributions of churning and blurring, and demonstrated that the impact of churning dominates. Furthermore, they found lower dispersion of angular momentum, 619 kpc km s^{-1} for 8 Gyr old populations, which corresponds to a lower value of radial migration of about 3.0 kpc compared to both Sanders & Binney (2015) and Frankel et al. (2018).

The results of the above studies are crucial, and are being used to interpret the observations. For instance, Sharma et al. (2020) used the dispersion of angular momentum from Sanders & Binney (2015) to explain the abundance dichotomy in [Fe/H]$-$[α/Fe] plane. They also demonstrated the need for churning in reproducing the dichotomy in their study. However, since the above determinations of strength of radial migration rely heavily on numerous simplifying assumptions, and models have several limitations and caveats (see sections 3.1, 5.5, and 6.6 of Frankel et al. 2020), it demands for constraints on radial migration from independent methods. Assuming our simulation sample is representative of Milky Way-like galaxies, we can use it to constrain radial migration in the Galaxy. In this section, we shall carefully analyse all six simulations to put an upper limit on the radial migration that took place for stars presently in the solar cylinder.

Sellwood & Binney (2002) defined radial diffusion caused by churning as radial migration. In practice, it is difficult to disentangle the contributions of churning and blurring, hence we defined radial migration of a star simply as the difference between its radial coordinates at present and birth locations, $R-R_{\rm birth}$. We emphasize that this definition includes contributions from both churning and blurring. Moreover, it has an ambiguity of measuring artificial radial migration for the stars born in highly eccentric orbits, i.e. this definition includes additional contributions on top of those from churning and blurring.

To alleviate the above ambiguity in the definition of radial migration, we shall consider only those stars in simulations that have relatively small orbital eccentricities, $e \lesssim 0.3$. In Fig. 8, we show eccentricities of the observed and simulation stars as a function of age. The eccentricities were estimated using `galpy`[4]

[4]http://github.com/jobovy/galpy

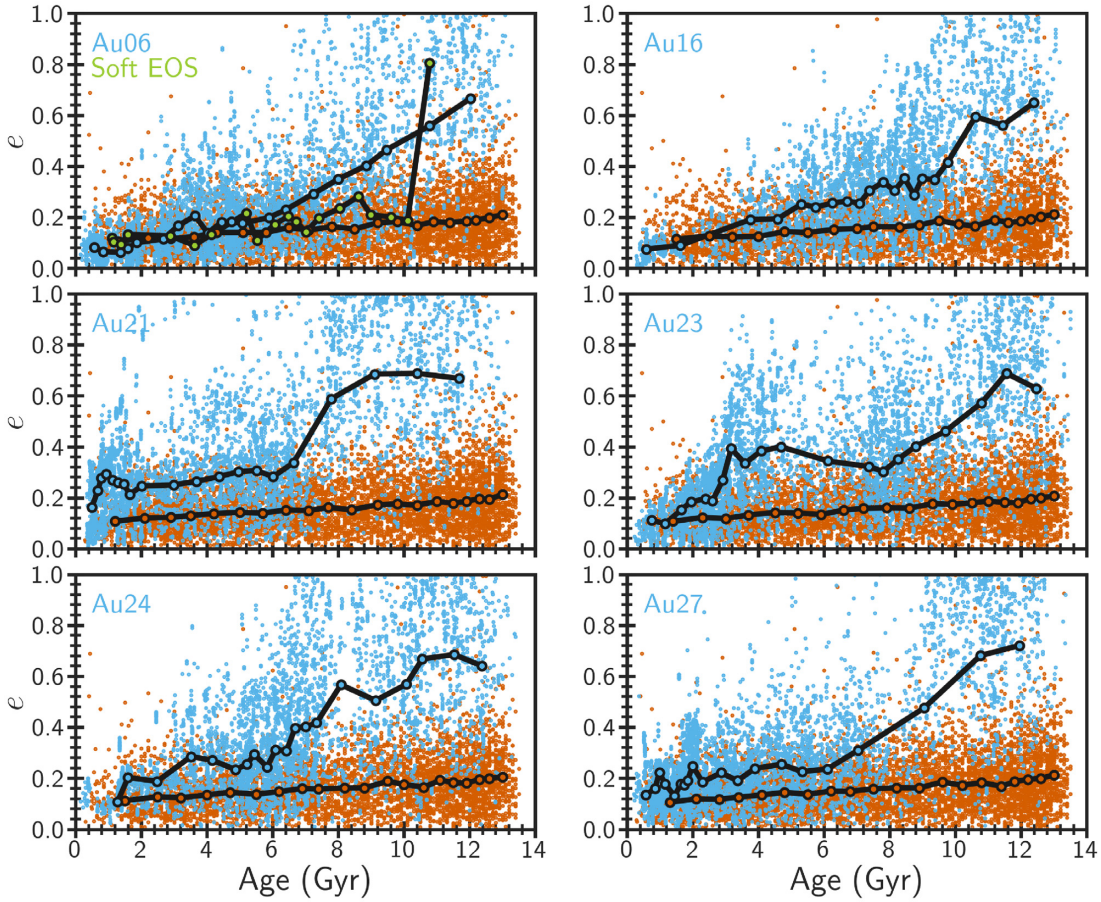

Figure 8. Orbital eccentricity of the observed and simulation stars as a function of age. The six different panels correspond to different simulations (see the legends) with the respective ICC catalogue generated assuming the standard solar azimuth. In each panel, the orange and blue dots represent the observed and simulation stars, respectively. To guide the eye, the orange, and blue filled circles connected with black lines show the binned median for the observation and simulations, respectively. In top left panel, the green filled circles connected with black lines show the model variation for Au06 as discussed in Section 3. The corresponding dots are not shown for the sake of clarity. The age bins were chosen in such a way that they contain approximately same numbers of stars.

assuming the Milky Way potential, `MWPotential2014`, from Bovy (2015). Note that there are small differences between the `MWPotential2014` and the simulation potentials, making the estimated eccentricities prone to systematic uncertainties. However, these estimates serve the purpose for us as they are used only to separate the late 'secular' evolution from the early turbulent evolution. As can be seen in the figure, older stars typically have large eccentricities, which is likely a result of their birth on highly eccentric orbits during the early merger dominated phase of galaxy formation and evolution. However, stars with ages less than 8 Gyr have median orbital eccentricities less than (or close to) 0.3 for all of the simulations, except possibly for Au21, for which stars of ages close to 8 Gyr have slightly larger eccentricities. Au21 underwent its most significant gas-rich merger at a lookback time of about 8 Gyr, leading to higher eccentricities around that time, while for the rest it happened at an earlier time (see fig. 2 of Grand et al. 2018a). Therefore, we shall only consider observed and simulation stars with ages less than 8 Gyr in this section. Note that the spatial distribution and spectral type of the observed and simulation stars, as discussed in Section 4, remain similar.

In Fig. 9, we show distributions of stellar migration predicted by all of the six simulations. To study its time dependence, we divided stars into two age bins: (1) young population with stellar ages less than 4 Gyr as shown by the continuous curves, and (2) old population with ages in the range [4, 8] Gyr as shown by the dashed curves. Note that, for all the simulations, the distributions are systematically wider for the older population than the younger one. This is expected because older stars have more time to migrate. In all panels, it is also interesting to note that the distributions corresponding to the four catalogues generated assuming different solar azimuths appear to be significantly different. This is mainly because of the differences in the distributions of the birth radius for the four catalogues (the distribution of the present-day radius remains approximately the same across catalogues because of the selection function). Note that since we have stars from different regions of the simulated galaxy for the four different catalogues, their birth profiles can differ due to the non-axisymmetric potential.

To quantify stellar migration, we again use the biweight mid-variance statistic to estimate the standard deviation of the distributions in Fig. 9, and denote it with ΔR. These estimates for both the young ($\Delta R_{<4}$) and old ($\Delta R_{\in[4,\,8]}$) populations are listed in Table 1 for all of the mock catalogues analysed in this study. The migrations predicted by the model variation for Au06 with softer equation of state are 1.07 and 1.72 kpc for the young and old populations, respectively. These are relatively smaller than the corresponding values predicted by the fiducial hotter Au06 simulation (see Table 1). We find maximum radial migration of 2.21 kpc (Au21) and 3.70 kpc (Au24) for the young and old populations,

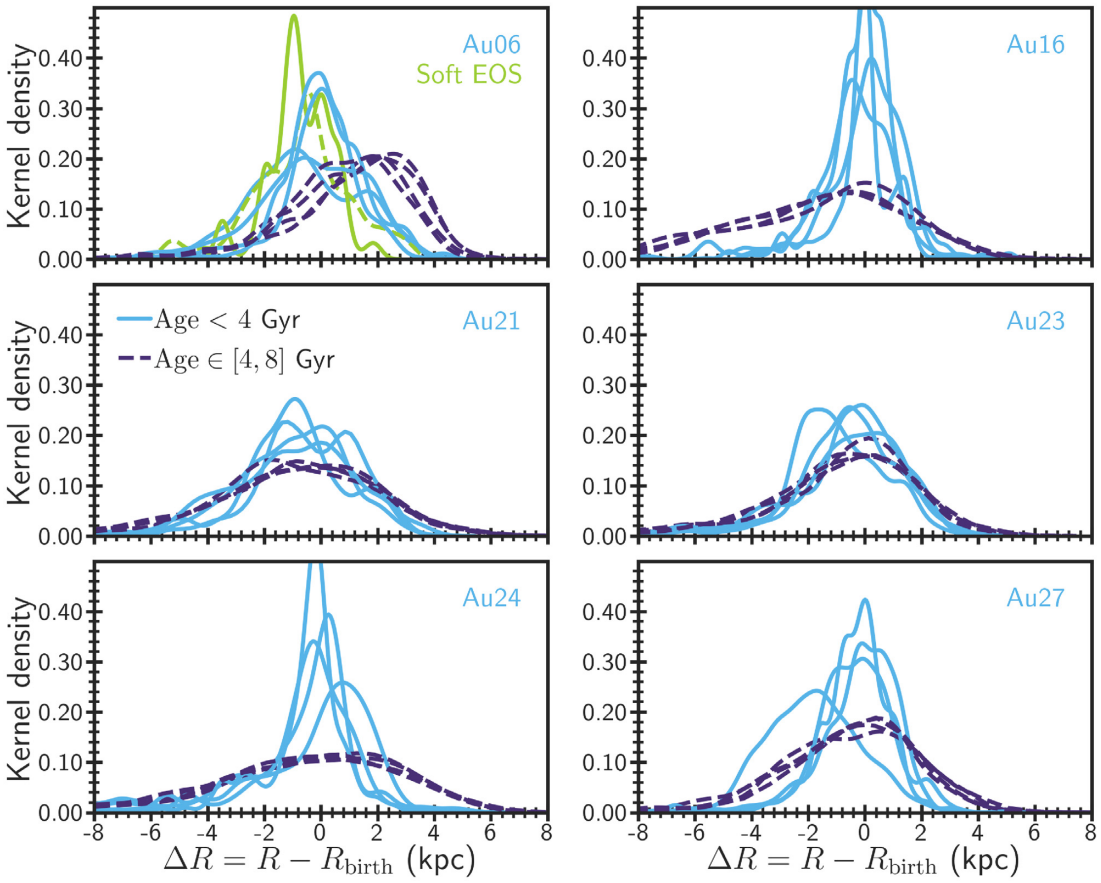

Figure 9. Distributions of radial migration predicted by all of the six simulations. The different panels correspond to the six different simulations (see the legends). In each panel, the four continuous curves show the distributions for the young populations (<4 Gyr) in ICC catalogues generated assuming different solar azimuths, while the four dashed curves demonstrate distributions for the old populations (∈[4, 8] Gyr). In top left panel, the green distributions show the model variation for Au06 as discussed in Section 3.

respectively. We emphasize that these estimates include contributions from churning, blurring and from the fact that stars could have been born with non-zero eccentricity. Moreover, since all of the Auriga simulations have hotter kinematics compared to the observations (see Figs 6 and 7), these values represent absolute upper limits on migration assuming its definition as given by Sellwood & Binney (2002), i.e. radial diffusion caused solely by churning.

We wish to point out one caveat here: the particle positions and velocities at birth were not directly output from the simulations, but instead were calculated during post-processing from snapshots of cadence of about 250 Myr. Therefore, the computed birth positions and velocities have associated uncertainties, especially for stars born during mergers when substantial movements happen at shorter timescales. However, since we consider only secular evolution in this section, such uncertainties should have only minor impact on the results.

The signatures of radial migration have been also identified in stellar elemental abundances. Particularly, the metallicity dispersion in the age–metallicity distribution traces the strength of radial migration – the larger the dispersion, the larger the migration (see e.g. Haywood 2006, 2008; Schönrich & Binney 2009). In Fig. 10, we show the metallicity dispersion as a function of age for all of the simulations and the observation. Recall that the observed orange curves may look slightly different depending on the catalogue and the simulation due to the selection function. To clearly see the relationship between the metallicity dispersion and radial migration, we note that the metallicity dispersion of Au16 is on average smaller than the other simulations as well as the observation for ages below 4 Gyr. This is in-line with our expectation as this simulation predicts lowest value of radial migration for the young population. As we can see in the figure, the Au21 metallicity dispersion on average matches closest with the observation for ages below 8 Gyr compared to the rest of the simulations. Therefore, it provides us estimates of radial migration of about 1.97 and 2.91 kpc for the young and old stellar populations, respectively. Note that these values are obtained by averaging the radial migrations listed in Table 1 for Au21 over catalogues generated assuming different solar azimuths. We wish to point out that the correlation between radial migration and metallicity dispersion depends on the underlying ISM metallicity gradient as a function of radius and time. For instance, a flatter radial gradient would cause a smaller metallicity dispersion even if there were a lot of migration. Although the absolute values of abundances predicted by the Auriga simulations differ significantly from the Milky Way, the gas-phase radial metallicity gradient tends to be negative at most epochs. Therefore, the relative trends should be qualitatively consistent with expectations for the Milky Way (based on the inside-out formation scenario and the current explanations for the flat age–metallicity relation for example).

The above findings indicate that the inferred radial migrations in Sanders & Binney (2015) and Frankel et al. (2018) are too high, whereas the one found in Frankel et al. (2020) is consistent with our study. Therefore, it would be interesting to see if a study similar to

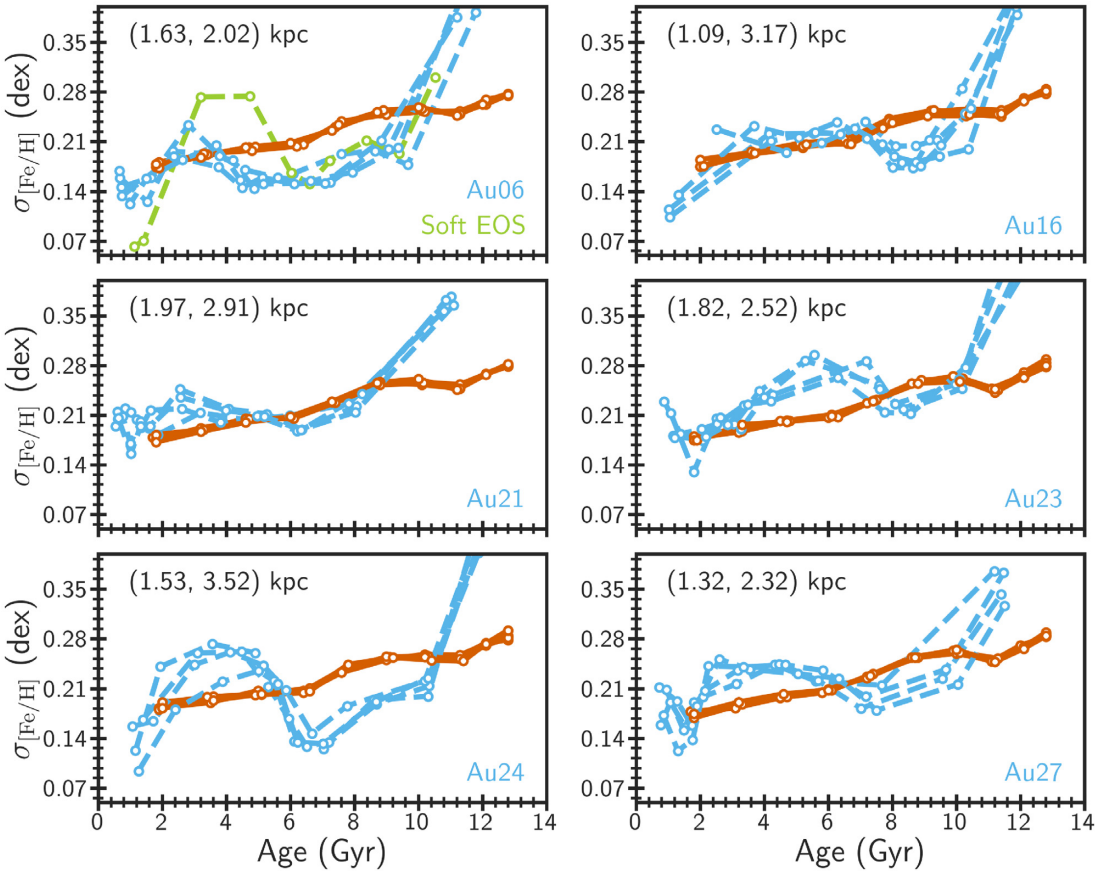

Figure 10. Metallicity dispersion as a function of age. The different panels correspond to the six different simulations (see the legends in the bottom right corners). In each panel, the solid orange curves represent observed samples (see the corresponding text for details), while the other blue dashed curves correspond to the ICC catalogues generated assuming different solar azimuths. In top left panel, the green curve shows the model variation for Au06 as discussed in Section 3. The age bins were chosen in such a way that they contain approximately same numbers of stars. The legends in the top left corner list radial migrations (averaged over catalogues with different solar azimuths) predicted by the simulations for the young (<4 Gyr) and old (∈[4, 8] Gyr) stellar populations, respectively.

Sharma et al. (2020) but with the spread in angular momentum from Frankel et al. (2020) can still reproduce the abundance dichotomy.

6 SUMMARY AND CONCLUSIONS

We compared six high-resolution cosmological zoom-in simulations of the formation of Milky Way-mass galaxies from the Auriga project with a variety of observations from the APOGEE survey, the *Kepler* satellite, and the *Gaia* mission. These simulations were a sub-set of a suite of 30 simulations for which mock *Gaia* DR2 stellar catalogues were available. Our observed sample consisted of 7186 stars for which high-fidelity spectroscopic, asteroseismic, and astrometric data were all available. In order to make meaningful comparisons, we applied detailed selection function, ensuring similar distributions of $J - K$ colour, K magnitude, and parallax for the observed and simulation stars. The process of applying the selection function resulted in two sub-samples – one of the observed sample, and the other of the mock catalogue at hand for comparison – in which stars had similar spatial distribution and spectral type.

We compared the elemental abundances in [Fe/H]−[Mg/Fe] plane. We found that simulations predict a variety of distributions in this plane, some of which also show a dichotomy. The abundance dichotomy for Au27 looks particularly similar to the observed data. Although simulations predict a dichotomy, we observe discrepancies when we look into the details of the observed and simulation abundance distributions. We also found that simulations tend to predict systematically higher metallicity compared to the observation. Some of these issues are likely to be related to the adopted yields in the simulations.

The simulation predictions for all three components of the Galactocentric velocity distributions were compared with the corresponding observed distributions. For all of the simulations, the predicted peak values of velocity distributions are in reasonable agreement with the observations. However, the fiducial Auriga simulations tend to systematically predict longer tails compared to the observed ones. The comparison of the vertical velocity dispersion as a function of age suggests significantly hotter kinematics in the simulated stars. However, a physics model variation that includes a softer equation of state for star-forming gas produces a set of chemo-dynamical properties in much better agreement with observations, illustrating the power of this framework to constrain galaxy formation models in the face of high-dimensional Galactic data.

We used all six simulations together with the observed data to put constraints on radial stellar migration in the solar cylinder. We defined stellar migration as the difference between the radial coordinates at present and birth positions. Assuming that simulations in our sample are representative of Milky Way-like galaxies, we estimated upper limits of 2.21 and 3.70 kpc for the strength of radial migration for young (<4 Gyr) and old (∈[4, 8] Gyr) stellar populations, respectively. The comparison of the metallicity dispersion as a

function of age between the observation and simulations suggests the strength of radial migration to be about 1.97 and 2.91 kpc for the young and old populations, respectively. We emphasize that our definition of radial migration includes contributions from churning, blurring and from the fact that some stars may be born on elliptical orbits. This means migration caused solely by churning must be smaller than the above values. Since some of the simulations reproduce the observed metallicity dispersion trend better in Fig. 10 than the others, it can be a promising diagnostic for distinguishing the formation and evolution histories.

Overall, we have developed a novel framework in which we address the challenging task of making systematic and unbiased comparisons between the rich contemporary observations and cosmological zoom-in simulations. We have also demonstrated the power of our technique by putting constraints on radial stellar migration. The current observed sample is limited to a small field of view (see Fig. 1); however, this can be greatly expanded using the K2 and TESS asteroseismic data. Our framework has great potential, and we shall apply it to future generations of simulations with different galaxy formation models to constrain the formation of the Milky Way.

ACKNOWLEDGEMENTS

We thank the anonymous referee for helpful comments. The authors would like to thank Volker Springel for inspiring discussions that led to the development of this project. Funding for the Stellar Astrophysics Centre is provided by The Danish National Research Foundation (grant agreement no. DNRF106). VSA acknowledges support from the Independent Research Fund Denmark (research grant 7027-00096B) and the Carlsberg Foundation (grant agreement no. CF19-0649).

DATA AVAILABILITY

The data underlying this article will be shared on reasonable request to the corresponding author.

REFERENCES

Adibekyan V. Z. et al., 2013, A&A, 554, A44
Agertz O. et al., 2021, MNRAS, 503, 5826
Ahumada R. et al., 2020, ApJS, 249, 3
Alam S. et al., 2015, ApJS, 219, 12
Anders F. et al., 2016, Astron. Nachr., 337, 926
Anders F. et al., 2017, A&A, 597, A30
Andrews B. H., Weinberg D. H., Schönrich R., Johnson J. A., 2017, ApJ, 835, 224
Astropy Collaboration, 2013, A&A, 558, A33
Astropy Collaboration, 2018, AJ, 156, 123
Aumer M., White S. D. M., Naab T., Scannapieco C., 2013, MNRAS, 434, 3142
Baglin A., Auvergne M., Barge P., Deleuil M., Catala C., Michel E., Weiss W., COROT Team, 2006, in Fridlund M., Baglin A., Lochard J., Conroy L., eds, ESA Special Publication, Vol. 1306, The CoRoT Mission Pre-Launch Status – Stellar Seismology and Planet Finding. ESA Special Publication, Noordwijk, the Netherlands, p. 33
Bedding T. R. et al., 2011, Nature, 471, 608
Bensby T., Feltzing S., Lundström I., 2003, A&A, 410, 527
Bensby T., Feltzing S., Oey M. S., 2014, A&A, 562, A71
Bird J. C., Loebman S. R., Weinberg D. H., Brooks A., Quinn T. R., Christensen C. R., 2021, MNRAS, 503, 1815
Bland-Hawthorn J., Gerhard O., 2016, ARA&A, 54, 529
Bovy J., 2015, ApJS, 216, 29
Brook C. B. et al., 2012, MNRAS, 426, 690
Brooks A. M. et al., 2011, ApJ, 728, 51
Buck T., 2020, MNRAS, 491, 5435
Buck T., Rybizki J., Buder S., Obreja A., Macciò A. V., Pfrommer C., Steinmetz M., Ness M., 2021, preprint (arXiv:2103.03884)
Casagrande L. et al., 2016, MNRAS, 455, 987
Casagrande L., Schönrich R., Asplund M., Cassisi S., Ramírez I., Meléndez J., Bensby T., Feltzing S., 2011, A&A, 530, A138
Christensen C., Quinn T., Governato F., Stilp A., Shen S., Wadsley J., 2012, MNRAS, 425, 3058
De Silva G. M. et al., 2015, MNRAS, 449, 2604
Fattahi A. et al., 2019, MNRAS, 484, 4471
Feltzing S., Bensby T., Lundström I., 2003, A&A, 397, L1
Fragkoudi F. et al., 2020, MNRAS, 494, 5936
Frankel N., Rix H.-W., Ting Y.-S., Ness M., Hogg D. W., 2018, ApJ, 865, 96
Frankel N., Sanders J., Ting Y.-S., Rix H.-W., 2020, ApJ, 896, 15
Freeman K., Bland-Hawthorn J., 2002, ARA&A, 40, 487
Fuhrmann K., 1998, A&A, 338, 161
Gaia Collaboration, 2016, A&A, 595, A1
Gaia Collaboration, 2018, A&A, 616, A1
Gilliland R. L. et al., 2010, PASP, 122, 131
Gilmore G. et al., 2012, The Messenger, 147, 25
Gilmore G., Reid N., 1983, MNRAS, 202, 1025
Gómez F. A., White S. D. M., Marinacci F., Slater C. T., Grand R. J. J., Springel V., Pakmor R., 2016, MNRAS, 456, 2779
Governato F., Willman B., Mayer L., Brooks A., Stinson G., Valenzuela O., Wadsley J., Quinn T., 2007, MNRAS, 374, 1479
Grand R. J. J. et al., 2017, MNRAS, 467, 179
Grand R. J. J. et al., 2018a, MNRAS, 474, 3629
Grand R. J. J. et al., 2018b, MNRAS, 481, 1726
Grand R. J. J. et al., 2020, MNRAS, 497, 1603
Grand R. J. J., Kawata D., Cropper M., 2015, MNRAS, 447, 4018
Green G. M., Schlafly E., Zucker C., Speagle J. S., Finkbeiner D., 2019, ApJ, 887, 93
Guedes J., Callegari S., Madau P., Mayer L., 2011, ApJ, 742, 76
Hayden M. R. et al., 2015, ApJ, 808, 132
Hayden M. R., Recio-Blanco A., de Laverny P., Mikolaitis S., Worley C. C., 2017, A&A, 608, L1
Haywood M., 2006, MNRAS, 371, 1760
Haywood M., 2008, MNRAS, 388, 1175
Hidalgo S. L. et al., 2018, ApJ, 856, 125
Holmberg J., Nordström B., Andersen J., 2009, A&A, 501, 941
House E. L. et al., 2011, MNRAS, 415, 2652
Howell S. B. et al., 2014, PASP, 126, 398
Huber D. et al., 2010, ApJ, 723, 1607
Huber D. et al., 2011, ApJ, 743, 143
Huber D., Stello D., Bedding T. R., Chaplin W. J., Arentoft T., Quirion P.-O., Kjeldsen H., 2009, Commun. Asteroseismol., 160, 74
Humphreys R. M., Larsen J. A., 1995, AJ, 110, 2183
Hunt J. A. S., Kawata D., Grand R. J. J., Minchev I., Pasetto S., Cropper M., 2015, MNRAS, 450, 2132
Jurić M. et al., 2008, ApJ, 673, 864
Karakas A. I., 2010, MNRAS, 403, 1413
Koch D. G. et al., 2010, ApJ, 713, L79
Lee Y. S. et al., 2011, ApJ, 738, 187
Lindegren L. et al., 2018, A&A, 616, A2
Lowing B., Wang W., Cooper A., Kennedy R., Helly J., Cole S., Frenk C., 2015, MNRAS, 446, 2274
Luri X. et al., 2018, A&A, 616, A9
Majewski S. R. et al., 2017, AJ, 154, 94
Marinacci F., Pakmor R., Springel V., 2014, MNRAS, 437, 1750
Martig M., Minchev I., Ness M., Fouesneau M., Rix H.-W., 2016, ApJ, 831, 139
Matteucci F., 2012, Chemical Evolution of Galaxies, Springer-Verlag, Berlin Heidelberg
Matteucci F., Greggio L., 1986, A&A, 154, 279
Michel E. et al., 2008, Commun. Asteroseismol., 156, 73
Mikolaitis, Š., de Laverny P., Recio-Blanco A., Hill V., Worley C. C., de Pascale M., 2017, A&A, 600, A22

Minchev I. et al., 2018, MNRAS, 481, 1645
Minchev I., Chiappini C., Martig M., 2013, A&A, 558, A9
Minchev I., Chiappini C., Martig M., 2014, A&A, 572, A92
Minchev I., Famaey B., 2010, ApJ, 722, 112
Minchev I., Martig M., Streich D., Scannapieco C., de Jong R. S., Steinmetz M., 2015, ApJ, 804, L9
Minchev I., Steinmetz M., Chiappini C., Martig M., Anders F., Matijevic G., de Jong R. S., 2017, ApJ, 834, 27
Naab T., Ostriker J. P., 2017, ARA&A, 55, 59
Nidever D. L. et al., 2014, ApJ, 796, 38
Nordström B. et al., 2004, A&A, 418, 989
Okamoto T., Eke V. R., Frenk C. S., Jenkins A., 2005, MNRAS, 363, 1299
Pillepich A. et al., 2018, MNRAS, 473, 4077
Pinsonneault M. H. et al., 2014, ApJS, 215, 19
Planck Collaboration XVI, 2014, A&A, 571, A16
Portinari L., Chiosi C., Bressan A., 1998, A&A, 334, 505
Recio-Blanco A. et al., 2014, A&A, 567, A5
Reid M. J., 1993, ARA&A, 31, 345
Ricker G. R. et al., 2014, in Oschmann J. M. J., Clampin M., Fazio G. G., MacEwen H. A., eds, Proc. SPIE Conf. Ser., Space Telescopes and Instrumentation 2014: Optical, Infrared, and Millimeter Wave. SPIE, Bellingham, p. 914320
Rix H.-W., Bovy J., 2013, A&AR, 21, 61
Roškar R., Debattista V. P., Quinn T. R., Stinson G. S., Wadsley J., 2008, ApJ, 684, L79
Salpeter E. E., 1955, ApJ, 121, 161
Sanders J. L., Binney J., 2015, MNRAS, 449, 3479
Sanderson R. E. et al., 2020, ApJS, 246, 6
Schaye J. et al., 2015, MNRAS, 446, 521
Schönrich R., Binney J., 2009, MNRAS, 396, 203
Schönrich R., Binney J., Dehnen W., 2010, MNRAS, 403, 1829
Sellwood J. A., Binney J. J., 2002, MNRAS, 336, 785
Serenelli A. et al., 2017, ApJS, 233, 23
Sharma S., Hayden M. R., Bland-Hawthorn J., 2020, preprint (arXiv:2005.03646)
Silva Aguirre V. et al., 2015, MNRAS, 452, 2127
Silva Aguirre V. et al., 2017, ApJ, 835, 173
Silva Aguirre V. et al., 2018, MNRAS, 475, 5487
Silva Aguirre V. et al., 2020, ApJ, 889, L34
Skrutskie M. F. et al., 2006, AJ, 131, 1163
Soubiran C., Bienaymé O., Siebert A., 2003, A&A, 398, 141
Spitoni E. et al., 2021, A&A, 647, A73
Spitoni E., Silva Aguirre V., Matteucci F., Calura F., Grisoni V., 2019, A&A, 623, A60
Spitoni E., Verma K., Silva Aguirre V., Calura F., 2020, A&A, 635, A58
Springel V., 2010, MNRAS, 401, 791
Springel V., Hernquist L., 2003, MNRAS, 339, 289
Steinmetz M. et al., 2006, AJ, 132, 1645
Stinson G. S. et al., 2013b, MNRAS, 436, 625
Stinson G. S., Brook C., Macciò A. V., Wadsley J., Quinn T. R., Couchman H. M. P., 2013a, MNRAS, 428, 129
van de Voort F., Pakmor R., Grand R. J. J., Springel V., Gómez F. A., Marinacci F., 2020, MNRAS, 494, 4867
Vogelsberger M., Genel S., Sijacki D., Torrey P., Springel V., Hernquist L., 2013, MNRAS, 436, 3031
Wang L., Dutton A. A., Stinson G. S., Macciò A. V., Penzo C., Kang X., Keller B. W., Wadsley J., 2015, MNRAS, 454, 83
Weinberger R. et al., 2017, MNRAS, 465, 3291
Woosley S. E., Heger A., 2007, Phys. Rep., 442, 269
Yu J., Huber D., Bedding T. R., Stello D., Hon M., Murphy S. J., Khanna S., 2018, ApJS, 236, 42
Zhao G., Zhao Y.-H., Chu Y.-Q., Jing Y.-P., Deng L.-C., 2012, Res. Astron. Astrophys., 12, 723
Zinn J. C., Pinsonneault M. H., Huber D., Stello D., 2019, ApJ, 878, 136

APPENDIX A: RESULTS FOR THE HITS CATALOGUES AND THE ICC CATALOGUES WITH NON-STANDARD SOLAR AZIMUTHS

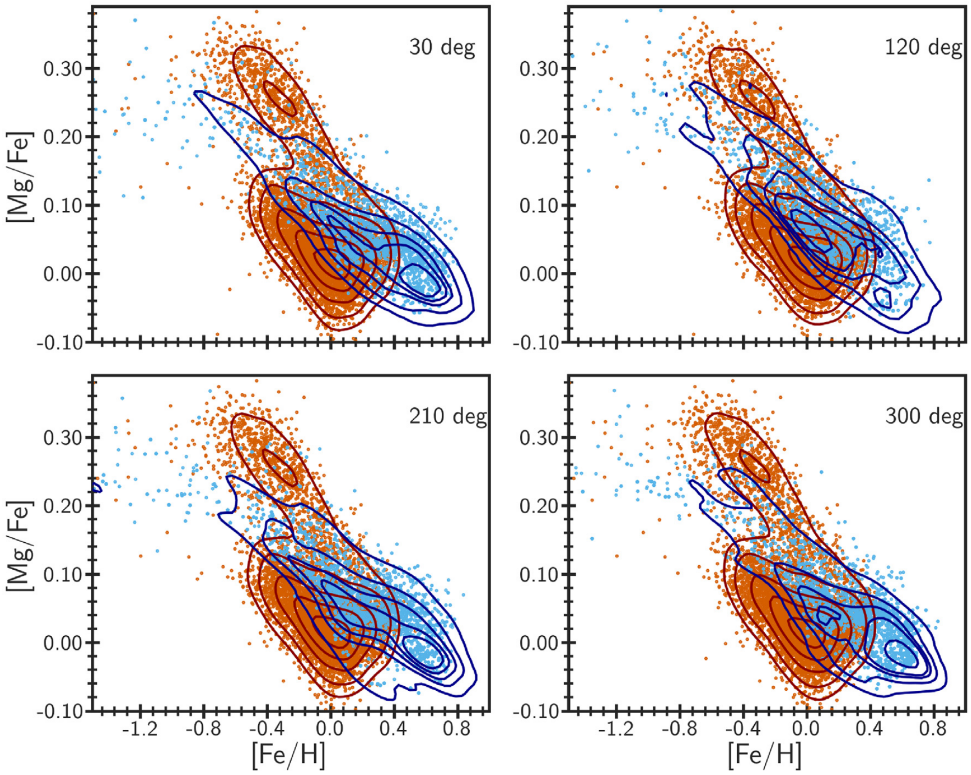

Figure A1. Same as Fig. 5 but contains only simulation Au06 with HITS catalogues generated assuming different solar azimuths (see the legends).

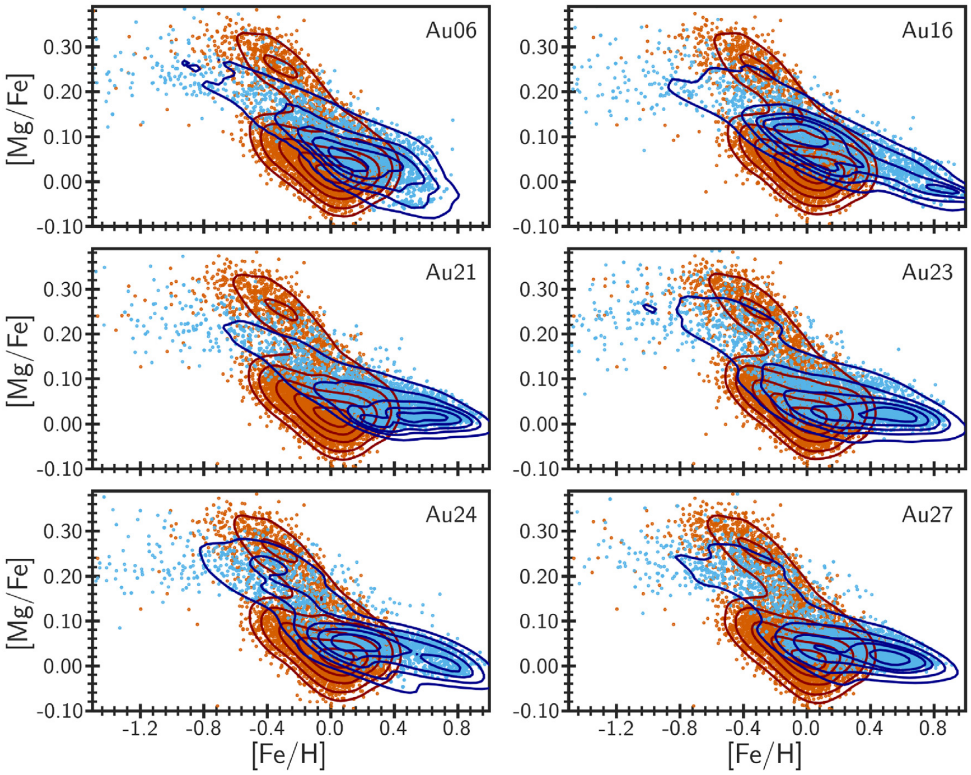

Figure A2. Same as Fig. 5 but with ICC catalogues generated assuming the solar azimuth at 120 deg behind the major axis of the bar.

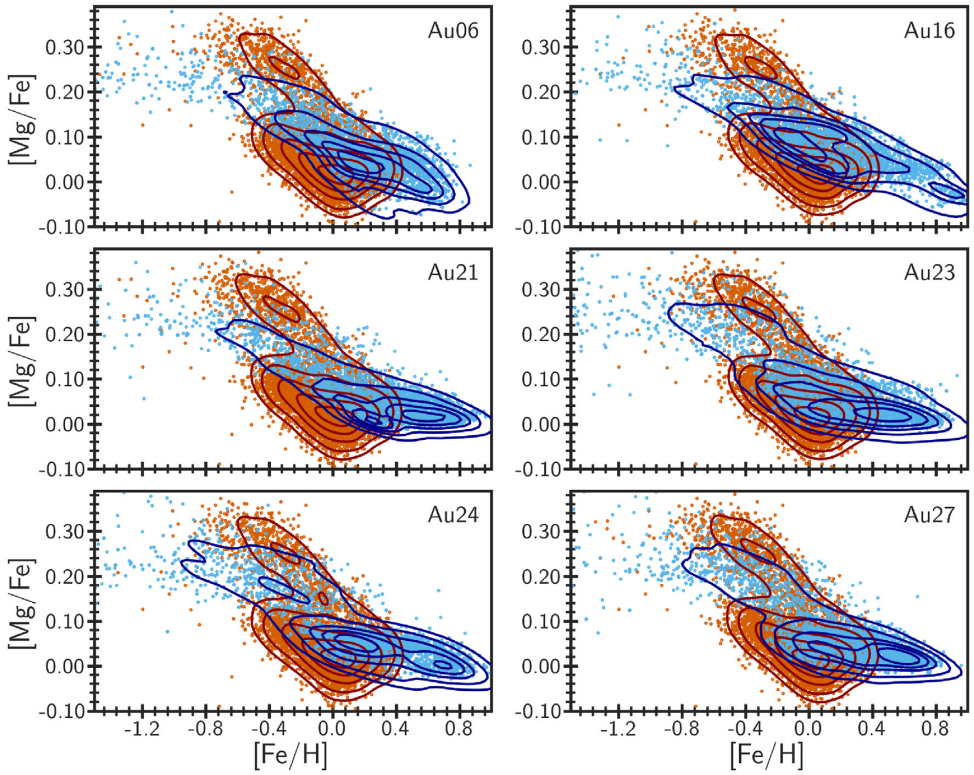

Figure A3. Same as Fig. 5 but with ICC catalogues generated assuming the solar azimuth at 210 deg behind the major axis of the bar.

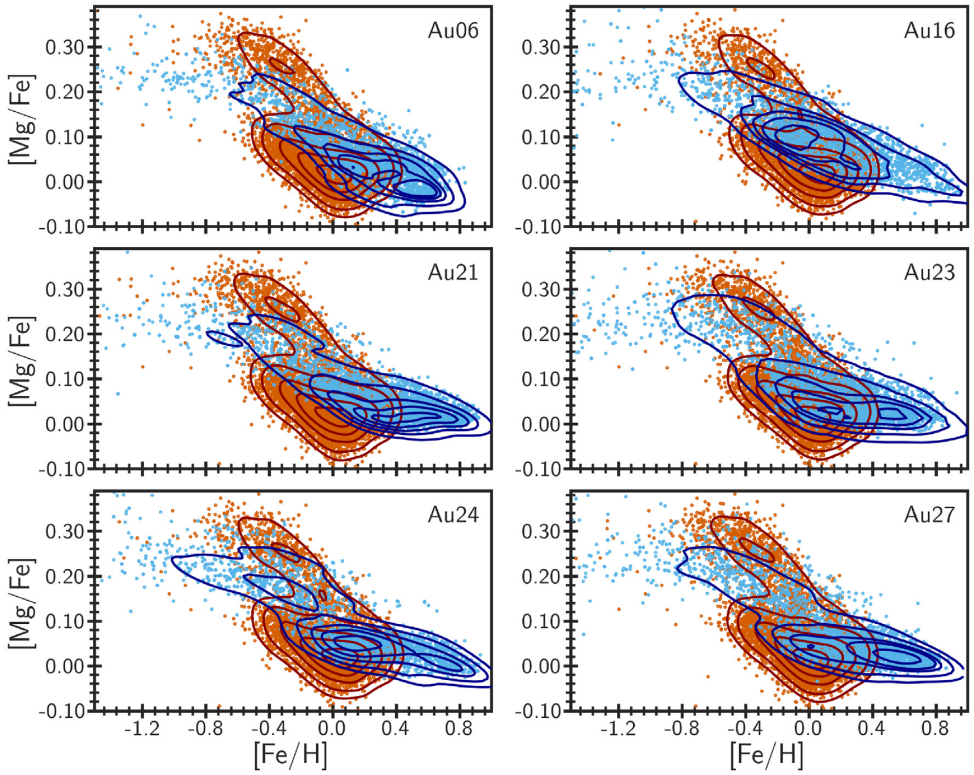

Figure A4. Same as Fig. 5 but with ICC catalogues generated assuming the solar azimuth at 300 deg behind the major axis of the bar.

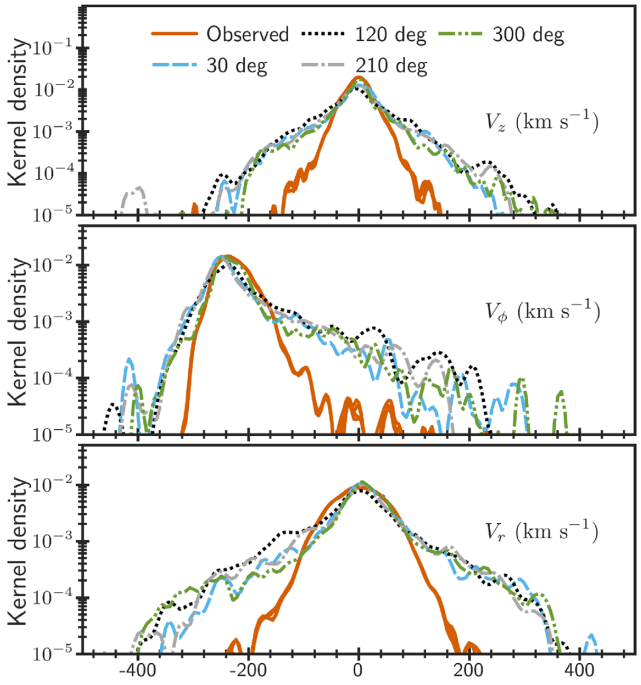

Figure A5. Same as Fig. 6 but contains only simulation Au06 with HITS catalogues generated assuming different solar azimuths (see the legends).

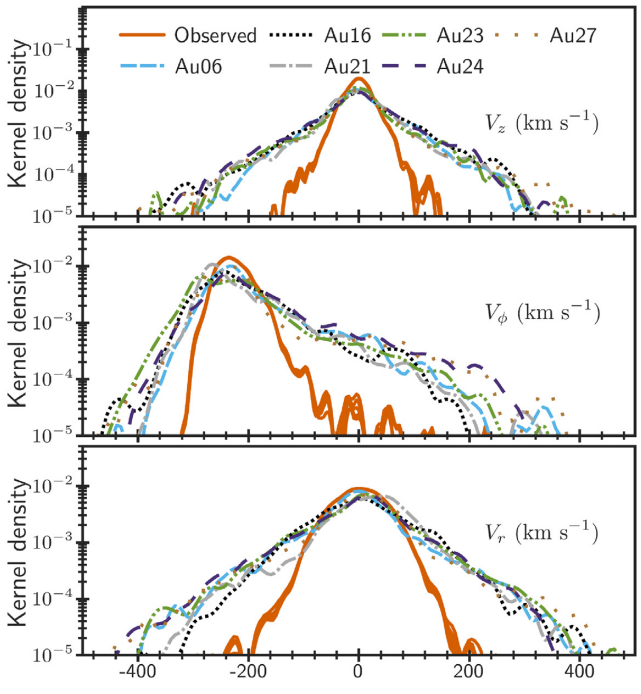

Figure A6. Same as Fig. 6 but with ICC catalogues generated assuming the solar azimuth at 120 deg behind the major axis of the bar.

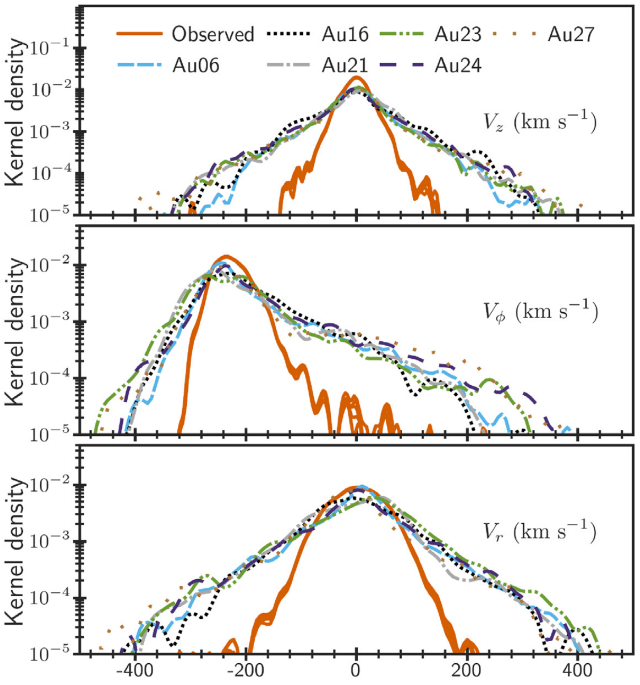

Figure A7. Same as Fig. 6 but with ICC catalogues generated assuming the solar azimuth at 210 deg behind the major axis of the bar.

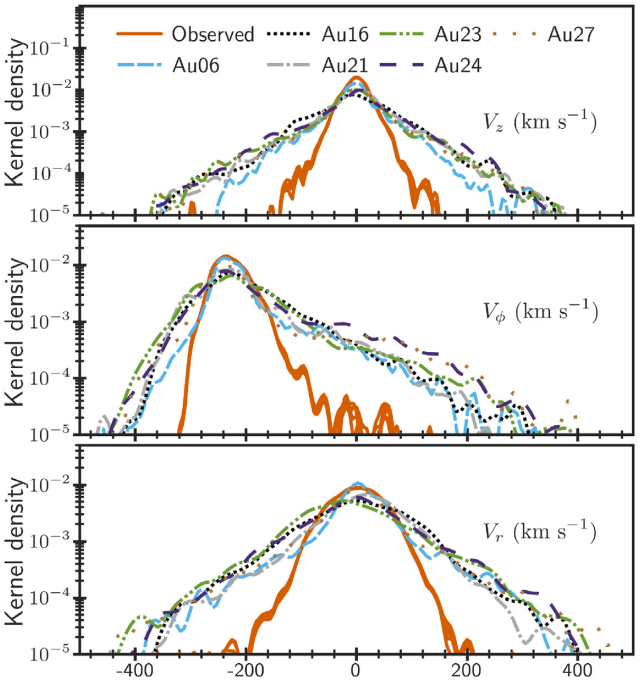

Figure A8. Same as Fig. 6 but with ICC catalogues generated assuming the solar azimuth at 300 deg behind the major axis of the bar.

This paper has been typeset from a TEX/LATEX file prepared by the author.